Microwave Radiometer RFI Detection Using Deep Learning

Priscilla N. Mohammed ⓘ, *Member, IEEE*, and Jeffrey R. Piepmeier ⓘ, *Fellow, IEEE*

Abstract—**Radio frequency interference (RFI) is a risk for microwave radiometers due to their requirement of very high sensitivity. The Soil Moisture Active Passive (SMAP) mission has an aggressive approach to RFI detection and filtering using dedicated spaceflight hardware and ground processing software. As more sensors push to observe at larger bandwidths in unprotected or shared spectrum, RFI detection continues to be essential. This article presents a deep learning approach to RFI detection using SMAP spectrogram data as input images. The study utilizes the benefits of transfer learning to evaluate the viability of this method for RFI detection in microwave radiometers. The well-known pretrained convolutional neural networks, AlexNet, GoogleNet, and ResNet-101 were investigated. ResNet-101 provided the highest accuracy with respect to validation data (99%), while AlexNet exhibited the highest agreement with SMAP detection (92%).**

Index Terms—**Deep learning, microwave radiometry, radio frequency interference (RFI), transfer learning.**

I. INTRODUCTION

RADIO frequency interference (RFI) detection in microwave brightness temperature data continues to be a problem of interest and several techniques have been developed to detect the presence of RFI in radiometer measurements, e.g., [1]−[10]. Soil Moisture Active Passive (SMAP) is the first spaceflight mission to use onboard digital signal processing dedicated to generating information to enable RFI detection and filtering [11]. The RFI detection algorithms in the SMAP ground processing are drawn from this previous work and include energy detectors in both time and frequency referred to as the pulse and cross-frequency detectors, the kurtosis method, which is a test for normality and polarimetric approaches, which search for anomalies in the third and fourth Stokes parameters [4], [12], [13]. These methods work best to filter RFI that is sparse in time and/or frequency. They improve the quality of measurements but at a cost of increased uncertainty or noise equivalent differential temperature due to removal of contaminated pixels, which reduces the time-bandwidth product.

Broadband radiometry enhances sensitivity by reducing instrument noise; thus, as upcoming sensors desire observations at much larger bandwidths than that of the SMAP radiometer

in unprotected or shared spectrum, RFI detection and filtering remains a necessity, e.g., [14], [15]. Indeed onboard RFI detection is being considered for future missions, for example, the second generation of polar orbiting meteorological satellites (MetOp-SG) as well as the Copernicus Imaging Microwave Radiometer mission [16], [17].

Increasing bandwidths lead to an increase in the number of spectral channels. Future instrument concepts include hyperspectral imagers and sounders that offer benefits such as increased precision and accuracy of products as well as extended spectral coverage [18], [19]. Thus, with the potential deluge of data from new sensors, conventional RFI detection and filtering may not be the only option. A new class of RFI detection algorithms includes intelligent approaches based on machine learning techniques. For example, the authors of [20] have used deep learning techniques to detect RFI in 2-D time ordered radio astronomy data and the authors of [21] have used deep learning to detect RFI in global navigation satellite system signals. Here, deep learning is used to demonstrate RFI detection on spectrograms produced by the earth orbiting SMAP microwave radiometer. The work in this article was done as a proof of concept to determine the feasibility of deep learning for RFI detection using real-world data. With the advent of graphics processing unit (GPU) technology for space use and the growing number of channels in digital receivers, it may be advantageous to run a deep learning algorithm on a GPU rather than conventional algorithms on a microprocessor.

II. METHODOLOGY

Deep learning [22] is a type of machine learning where the model learns to perform classification tasks directly from images, text, or sound [23], [24]. In this work, RFI detection is investigated using supervised learning based on SMAP spectrograms. The model is trained using labeled datasets as inputs and the training process is done iteratively until the expected output is generated. Convolutional neural networks (CNNs) have been successfully exploited in image classification and most commonly used in this type of application [25], [26]. Transfer learning [27] is the process where a pretrained network is fine-tuned; the learned features are transferred to a new task using a smaller number of training images and is usually much faster. The CNN could be trained using simulated RFI; however, SMAP measurements were chosen for this proof of concept experiment. Although millions of spectrogram images can be produced from SMAP data, transfer learning is utilized for this application to produce results in a timely manner for study.
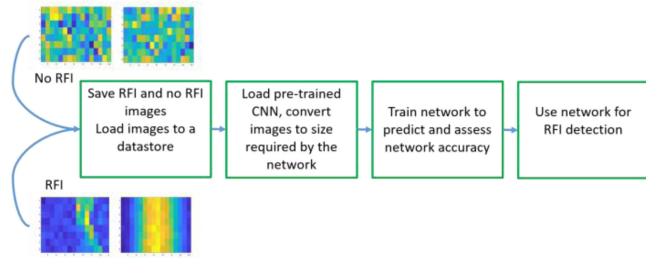
Fig. 1.   Algorithm workflow.

To use deep learning and transfer learning for RFI detection, the problem is defined as an image classification one where spectrograms are the input images to be classified as having RFI or not having RFI. In this article, the benefits of transfer learning are leveraged and the pretrained CNNs AlexNet [25], GoogleNet [28], and ResNet-101 [29] were used for feature learning and classification. These networks were previously trained on more than a million images from the ImageNet [30] database to classify images into 1000 categories including nature, animals, and everyday objects.

The transfer learning approach applies knowledge of one type of problem to a different but related problem. In order to use an existing CNN such as AlexNet to detect objects not trained in the original network, it can be retrained through transfer learning. The last few layers of the network were replaced and then retrained with images of spectrograms derived from SMAP data. In the proposed method here (see Fig. 1), the pretrained network was loaded using Matlab, labeled input images were loaded to a datastore that stores the file paths to read the image data into memory as needed and the image size converted to that required by the existing network. The last layers of the CNN that learn features specific to the input dataset were replaced and the network was then trained using 80% of the input spectrogram images. The network was validated using 20% of the input data and the results were deployed to classify new images.

A. Data Acquisition for Input Training Images

Each SMAP footprint in the Level 1A data contains an 8 (1.2-ms samples) $\times$ 16 (1.5-MHz channels) spectrogram of antenna counts or average power [31]. The passband shape is equalized by applying independent gain and offset calibration coefficients to each of the 16 frequency channels [32]. The spectrograms were converted to images, with normalized color scales, and used as inputs to the deep learning algorithm implemented in Matlab.

Supervised training requires *a-priori* labeling of the images; in this case, "no RFI" and "RFI." RFI cases were taken from all parts of the globe including low level ($5-10$ K), moderate level ($10-100$ K), and high level (>100 K) RFI as well as different types of RFI such as pulsed, CW, and wideband. Ground truth is difficult to establish when using real-world data; thus, conditions were set where it is reasonably certain that RFI is present in the footprint. The SMAP ground processing algorithm, which detects and filters RFI, attempts to estimate the RFI strength. RFI level is determined from the difference of nonfiltered and filtered

data. However, when RFI is very strong (typically > 400 K), 100% of the spectrogram is blanked resulting in a reported null value for the filtered footprint. In these cases, RFI level cannot be directly determined. Also, if more than 50% of the spectrogram is blanked by the algorithms, it is reasonably certain that RFI exists in that footprint regardless of the difference of the nonfiltered and filtered data. Therefore, spectrograms were labeled as "RFI" on the condition that either the RFI level for the footprint was over 5 K [-20 dB interference to noise ratio (INR)] as estimated by the SMAP ground processing algorithms or that the SMAP ground processing algorithms blanked more than 50% of the spectrogram.

To be confident that the RFI-free cases were indeed not contaminated, RFI quiet parts of the globe were used for these samples. Footprints over Australia, Antarctica, the Arctic, and the Southern part of the Indian Ocean were used with the condition that the RFI level was less than 2 K and the number of pixels flagged was less than 50% of the spectrogram. The training input data consisted of 2507 images labeled "RFI" and 2507 images labeled "no RFI" with 80% used for training and 20% for validation. Orbits different to those used for obtaining training samples were used to test the trained networks.

B. Training the Network

CNNs consist of convolution and pooling layers that extract features from the image inputs followed by a classification layer that uses the features to classify the input image. In transfer learning, most of the convolutional part is unchanged and the new classifier replaces the classification layer. The last learnable layer was replaced with a fully connected (FC) layer with the number of outputs equal to the number of classes in the input dataset. In this case, the number of classes is two since the objective is to classify images as "RFI" or "no RFI." The first layer of the network is the image input layer that specifies the image size. The training images were resized and additional augmentation prevented the network from overfitting. Random translation and reflections of the spectrograms were performed which represent shifting RFI in time and frequency. Once training was completed, accuracy was determined by classifying the validation images with the trained network.

In this study, three well-known CNN architectures, AlexNet, GoogleNet, and ResNet-101, have been analyzed for classification precision and training time. These pretrained networks, which have already learned to extract features from images of nature, were used as a starting point to learn the new task of RFI detection using SMAP data as inputs. Transfer learning was first done using AlexNet since this network is one of the faster networks. Once the settings for training were established, the other networks, which are known to be more accurate but with longer prediction times, were used to check for better accuracy and to see if RFI detection results improved.

AlexNet contains 25 distinct layers that includes five convolutional layers and three FC layers in which a rectified linear unit (ReLu) activation function is applied after every convolutional and FC layer. Layer 1 is the input layer to which the images are fed. Layers 2-22 are the convolution, ReLu, and Max Pooling layers where feature extraction occurs. The last three layers
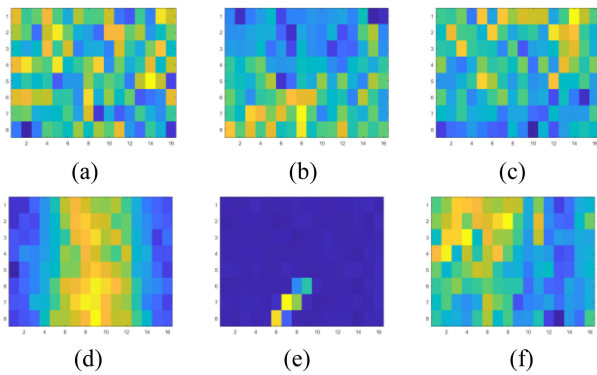
Fig. 2. (a)−(c) are examples of RFI-free images over Australia, where (a) is over land and (b) and (c) are coastline footprints. The bottom images, (d)−(f), are examples of RFI contaminated footprints over Japan, the United Kingdom, and Spain, respectively.

include the FC layer that maps the extracted features to each of the two output classes in this experiment (RFI; no RFI), followed by the softmax layer where the probability is assigned to the input image for each output class and lastly the classification layer returns the output class of the input image. The first two FC layers have 4096 neurons and the third has 1000. GoogleNet and ResNet-101 are 22 layers and 101 layers deep, respectively. Both contain an FC layer of 1000 neurons.

The input image size for AlexNet is $227 \times 227 \times 3$ and $224 \times 224 \times 3$ for the other two CNNs used. During the transfer learning process, only the last three layers were modified to suit the RFI classification problem.

III. EXPERIMENTS

The general hypothesis is that the object-recognition capabilities of the CNN will detect RFI features in the spectrogram amidst the random variations of natural thermal emission, much like detecting a specific object in a busy image. The RFI-free images over uniform scenes are essentially random fields with normally distributed values. Spectrograms with RFI tend to have features concentrated in time or frequency and in some cases have broad time-frequency features that can mimic geophysical features such as coastlines. Nonuniform scenes, e.g., coastlines, impose a systematic variable background on the spectrogram over time, which, as it turns out, can be mistaken for RFI. Therefore, two groups of experiments with different training datasets were run. The first group included RFI-free coastlines in the training set. The second group excluded RFI-free coastlines in the training set and concentrated on using RFI-free data from uniform scenes. Fig. 2 shows some examples of RFI-free (a−c) and RFI-contaminated (d−f) footprints. Fig. 2(a) shows a natural, uniform scene and (b) and (c) are examples of nonuniform coastal crossings. Fig. 2(d) shows RFI continuous in time and limited in frequency; Fig. 2(e) shows an RFI signal chirped in frequency and (f) shows RFI with less distinct time-frequency definition.

Including coastlines in the RFI-free training set [e.g., Fig. 2(b) and (c)] can result in missed detections of RFI such as Fig. 2(f) because it is similar to (c). On the other hand, training the CNN

TABLE I
RESULTS SHOWING THE ACCURACY FOR EACH NETWORK AS WELL AS THE TRAINING TIMES

Network	Accuracy 1 (%)	Accuracy 2 (%)	Training Time 1 (Hr)	Training Time 2 (Hr)
AlexNet	98.5	96.5	7.73	7.10
GoogleNet	97.8	98.3	16.21	16.19
ResNet-101	98.6	98.9	31.62	31.00

Note: Each network was trained twice: dataset 1 contained coastlines in the RFI-free images while dataset 2 did not.

TABLE II
RESULTS SHOWING THE CONFUSION MATRIX FOR EACH NETWORK FOR THE VALIDATION DATASET

Network			Confusion 1 (%)		Confusion 2 (%)	
AlexNet	True	RFI	97.8	2.2	99.4	0.6
	Class	no RFI	0.8	99.2	6.4	93.6
GoogleNet	True	RFI	95.8	4.2	96.8	3.2
	Class	no RFI	0.2	99.8	0.2	99.8
ResNet-101	True	RFI	97.6	2.4	98	2
	Class	no RFI	0.4	99.6	0.2	99.8
			RFI	no RFI	RFI	no RFI
			Predicted Class		**Predicted Class**	

Note: **The** true class indicates that the true classification and the predicted class is that of the trained network. **Dataset 1** contained coastlines in the **RFI-**free images, while dataset 2 did not.

using data with RFI such as that shown in Fig. 2(f) can produce false alarms along coastlines. To complete the experiment, the two trained networks were then tested with data taken from orbits over Europe and the Middle East to test RFI detection performance.

IV. RESULTS

A. Accuracy of the Trained CNNs

In this section, the performance of the trained CNNs to identify RFI is presented. Table I shows the results of a comparative analysis with respect to training time and the accuracy using validation data. Each network was trained with 80% of the labeled training dataset and the remaining 20% was used to test for accuracy. The results show that AlexNet had the least training time of the three and ResNet-101 took the longest. Each network was trained twice, using datasets with and without coastlines in the RFI-free images. The training times were slightly less using the second dataset and accuracies were slightly better for GoogleNet and ResNet-101. All networks in both training cases achieved over 96% accuracy. Table II shows the confusion matrix for each trained network. The lower left and upper right of the off-diagonal represent the probability of false alarm and probability of missed detection respectively. In order to test these networks for RFI detection, an orbit over Europe and another over the Middle East were used. These orbits were different to the orbits used for the training data extraction.

B. Test Orbits

The orbits over Europe and the Middle East were chosen as test cases for the trained networks based on the types of RFI seen in these locations of the world. The pass over Europe
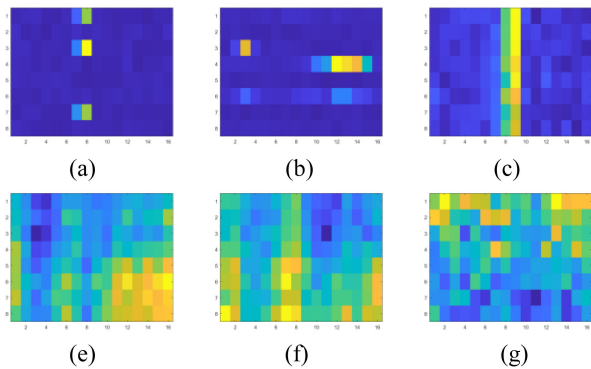
Fig. 3. Spectrograms from the orbit over Europe showing typical RFI in this pass (a), (b), and (c). The RFI is either sparse in time or frequency. Spectrograms from the orbit over the Middle East, (e), (f) and (g) indicate wideband RFI.

TABLE III
RESULTS SHOWING THE DETECTION AGREEMENT WITH SMAP DETECTION FOR EACH NETWORK

Network	Europe Orbit Agreement with SMAP detection (%)	Middle East Orbit Agreement with SMAP detection (%)
AlexNet	97.58	88.31
AlexNet (no coast)	98.85	92.23
GoogleNet	95.89	82.10
GoogleNet (no coast)	96.84	85.03
RestNet-101	96.09	85.77
Restnet-101 (no coast)	97.09	88.05

consisted mostly of pulsed RFI, which is sparse in time and frequency, while the RFI over the Middle East was mostly wideband and more persistent in time and frequency. Fig. 3 shows the spectrograms of sample footprints from these orbits. The example spectrograms over Europe show RFI that is narrowband and pulsed, wideband pulsed, and narrowband continuous. The spectrograms over the Middle East contain wideband RFI concentrated over a large portion of the footprint with one RFI example [Fig. 3(g)] that looks very similar to a coastline feature. The feature in Fig. 3(g) was identified as RFI-contaminated since multiple detectors in the SMAP algorithms flagged several pixels and the footprint was anomalously high in brightness temperature. This highlights the problem that the deep learning detector faces when identifying RFI-contaminated images versus RFI-free geophysical features.

Parts of both orbits with RFI concentration were tested using the trained networks and the RFI detection results were compared to SMAP RFI detection. Since the SMAP ground processing contains numerous detectors with a combined false alarm rate of ~6% [13], the same conditions for creating the RFI contaminated footprints for training data were used as the conditions for positive SMAP RFI detection. Thus, if a footprint had an RFI level greater than 5 K or the SMAP algorithms blanked more than 50% of the spectrogram, then that footprint was positively identified as RFI contaminated and compared to the binary results from the trained networks.

C. RFI Detection Results

For the Europe orbit, 19 405 footprints were tested and 4088 footprints fit the SMAP detection criteria. For the orbit over the Middle East, 98 467 footprints were tested and 3113 footprints were detected by the SMAP detection. Table III shows how well the trained networks detected RFI over the two test orbits compared to SMAP detection. All the networks had similar detection agreement rates for the Europe orbit. This indicates that the deep learning algorithm has high performance for detecting pulsed and narrowband RFI. The networks showed lower performance for detecting RFI over the Middle East where wideband signatures are more prevalent. However, the detection agreement increased when coastlines were excluded from the

RFI-free training dataset. This increase was more prominent for the test orbit over the Middle East where AlexNet showed the highest detection agreement with SMAP detection.

D. Europe Orbit

Fig. 4(a) shows the horizontal polarization brightness temperatures for part of the orbit over Europe that was tested. RFI shows up as hot spots throughout the image. Any value greater than 330 K can automatically be considered as RFI since this is the geophysical limit for brightness temperature measurements. The results of the deep learning algorithm (with coastlines in the RFI-free training dataset) are shown in Fig. 4(b). The RFI detected footprints were omitted and appear gray in the image. The results compared to SMAP detection are shown in Fig. 4(c). The red pixels indicate deep learning and SMAP detection agreement of RFI contaminated footprints with gray showing agreement of RFI-free footprints. Blue shows deep learning detection but no SMAP detection, and yellow shows SMAP detected footprints not detected by deep learning. Of the 19 405 footprints tested in this orbit, 4088 fit the SMAP detection criteria stated in Section II-A. The deep learning algorithm has a 97.58% (3989 footprints) agreement with these SMAP detected footprints, depicted as red in Fig. 4(c). The deep learning algorithm detected an additional 3418 footprints as RFI contaminated which are blue in Fig. 4(c).

Not all the additional footprints were false detections. Manual inspection revealed low level pulsed sources less than 5 K. Some were false alarms. Since SMAP has an FAR of ~6%, this implies that about eight spectrogram pixels are flagged on average in the absence of RFI by the SMAP detection algorithms. Deep learning detected 256 footprints (1.3% of total tested footprints) that had 10 or fewer pixels detected by the SMAP algorithms. These footprints can be considered false alarms. When AlexNet (no coastlines) was used for testing, agreement with SMAP detection increased to 98.85%, but the number of footprints detected as possible false alarms also increased to 1053 or 5.4% of the tested footprints.
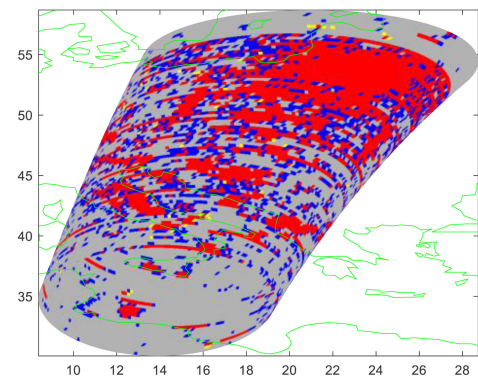
E. Middle East Orbit

Fig. 5 shows the results of a similar analysis over the Middle East. Using the training network AlexNet, the deep learning algorithm has 88.31% (2749 footprints) agreement with SMAP detection (3113 footprints). The agreement increased to 92.23%
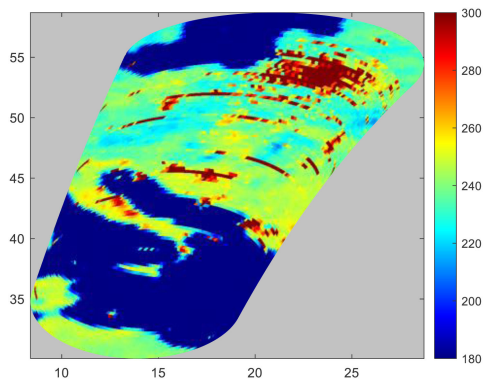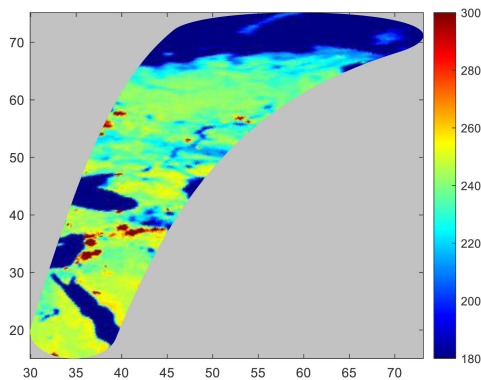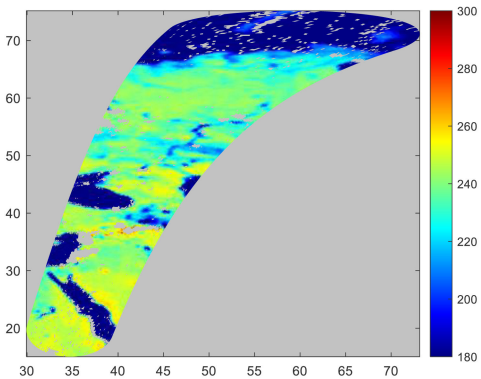
(a)
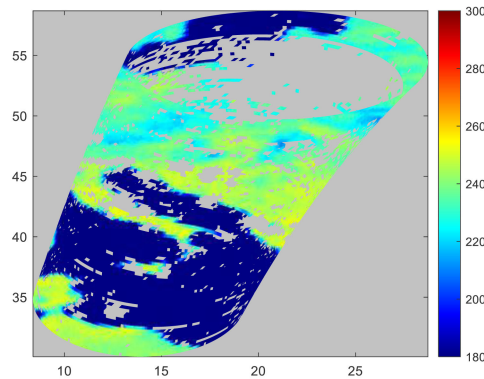
(b)

(c)

Fig. 4.   (a) Horizontal polarization brightness temperature for the test footprints over Europe. The color scale was limited to values from 180 to 300 K. Footprints with brightness temperature equal to or lower than 180 K appear dark blue and those that are 300 K and above are dark red. Footprints detected by the deep learning algorithm using AlexNet (b) were removed from the images. A comparison of SMAP detection and deep learning are shown in (c).

(a)

(b)

(c)

Fig. 5.   (a) Horizontal polarization brightness temperature for the test footprints over the Middle East. (b) Footprints detected by the deep learning algorithm using AlexNet (no coast) were removed from the images. (c) A comparison of SMAP detection and deep learning.
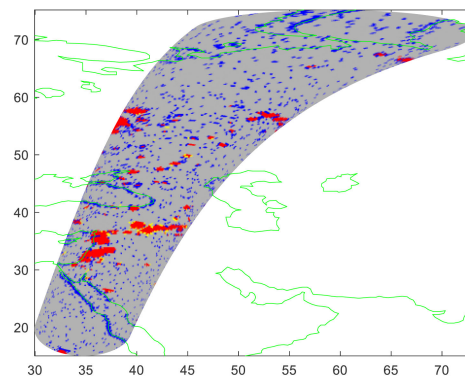
(2871 footprints) when AlexNet (no coast) was used. The number of false alarm detections also increased from 551 (0.6%) to 4470 (4.54%) footprints (see Table IV). When Fig. 5(c) is examined, there appears to be footprints detected by the deep learning algorithm concentrated along the coasts that do not match SMAP detection. Random mismatches occur throughout the orbit as well. There are 8119 additional footprints (shown

TABLE IV
RESULTS SHOWING THE FOOTPRINTS CONSIDERED FALSE ALARMS FOR RETRAINED ALEXNET WITH DIFFERENT INPUT TRAINING SETS

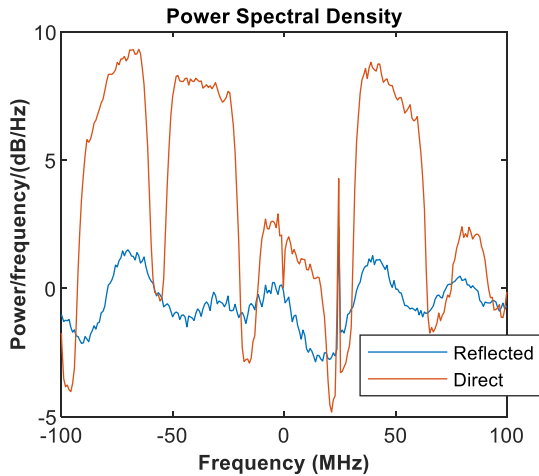| Network	Europe Orbit False Alarm Footprints	Middle East Orbit False Alarm Footprints
AlexNet	256 (1.3 %)	551 (0.6 %)
AlexNet (no coast)	1053 (5.4 %)	4470 (4.54 %)

Fig. 6. Power spectral density of the normalized baseband signals measured with the K-band recording system deployed at Platform Harvest.
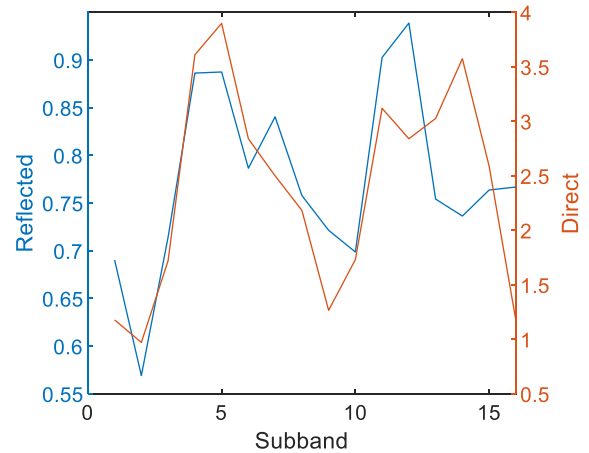

Fig. 7. Normalized variance of the baseband signals after spectral subbanding measured with the K-band recording system deployed at Platform Harvest.
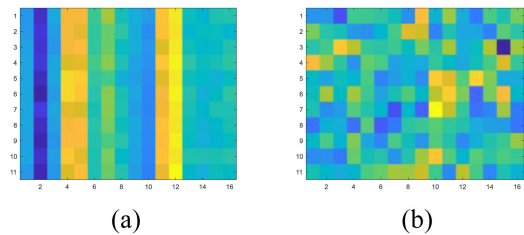

Fig. 8. Example spectrograms of the reflected DBS signal (a) and RFI-free data (b) tested by SMAP-trained deep learning networks.

in blue) detected by deep learning that do not match the SMAP detection criteria imposed. Footprints that appear as yellow in Fig. 5(c) are deep learning missed detections. These test cases indicate that the deep learning algorithm is directly affected by the input training data. The deep learning algorithm provided very good detection for RFI that is localized in time or frequency since RFI data has very distinct features when compared to RFI-free data.

This study produced a lower detection rate for broadband RFI as indicated by the results of the Middle East test orbit. This orbit contained RFI, which was mostly broadband in nature and even contained RFI with characteristics similar to geophysical features. This allowed for higher missed detections or higher false alarms depending on whether coastlines were included in the input training data.

V. APPLICATION TO A NEW INSTRUMENT

In this section, the SMAP-trained networks were used to detect RFI in data produced by a second, unrelated, instrument. Over the period of August 2−6, 2017, a reflectometry experiment took place at Platform Harvest located about 10 km off the coast of central California [33]. Direct and reflected signals from DirecTV, a US-based direct broadcast satellite (DBS) service provider, were measured with a K-band system [34]. The K-band system included an RF front end with two commercial reflector antennas and low-noise block-down converters and a digital back end designed to collect 200 MHz of bandwidth from 18.6 to 18.8 GHz. Of particular interest are ocean reflections that can affect sensors in this frequency range. The global precipitation measurement (GPM) microwave imager (GMI) has seen RFI caused by ocean reflections from DBS signals at 18.7 GHz which is a shared allocated band [35].

Fig. 6 shows the normalized power spectral density of the direct and reflected DBS signals measured by the K-band system with INRs estimated at 10 and −8 dB, respectively [34]. The INR is relatively high; thus, the deep learning detector is expected to work well. Fig. 7 shows a time slice of the normalized variance

of the direct and reflected signals after spectral subbanding. The reflected signal retains a similar shape to the direct signal, but the power level is much lower. The time frequency power for the reflected signal was converted to spectrogram images as was done with SMAP data in this study.

The K-band digital back end provided data products including power for 16 spectral subbands for both direct and reflected signals with a time resolution of approximated 328 μs. Spectrograms were created using 11 (328-μs samples) × 16 (12.5-MHz channels) for an elapsed time of 3.6 ms and total bandwidth of 200 MHz, which approximately matches the total integration time and bandwidth of the GMI 18.7-GHz channel [36].

Approximately, 70 s of data were used to create 19 194 images for test. Data without RFI was obtained by placing absorber in front of the antenna of the K-band system. Spectrograms for the no-RFI case were created similarly with 10 s of absorber data providing 2636 images.

A spectrogram with the reflected DBS signal is shown in Fig. 8(a), which shows distinct features of the RFI occurring continuously and concentrated in frequency. Fig. 8(b) is an example of spectrogram data without RFI taken by the K-band system. The SMAP-trained networks in Table III were used to test these RFI contaminated and RFI-free images. All the networks classified 100% of the images with reflected DBS signals as RFI contaminated. This is not surprising since the DBS signal is easily identifiable in the images. Half of the networks classified 100% of the noncontaminated images as RFI-free.

TABLE V
RESULTS SHOWING THE CLASSIFICATION OF RFI-FREE IMAGES FROM THE
K-BAND SYSTEM

Network	Images classified as RFI free
AlexNet	2636 (100%)
AlexNet (no coast)	2629 (99.73%)
GoogleNet	2636 (100%)
GoogleNet (no coast)	2635 (99.96%)
RestNet-101	2636 (100%)
Restnet-101 (no coast)	2634 (99.92%)

The other networks falsely classified seven (0.27%) or less of the RFI-free images as RFI contaminated. See Table V for the results of this classification.

This classification experiment demonstrates that networks can be trained with data from one sensor or several data sources and used to detect RFI in other data sources. The deep learning algorithm learned features of different types of RFI seen in SMAP data and was able to correctly detect these features from the K-band system dataset.

VI. CONCLUSION

In this article, a transfer learning approach for RFI detection using SMAP detection was presented. In this approach, the last few layers of pretrained networks were replaced and retrained with a smaller dataset. These results were then used to classify images from two test orbits of SMAP data. Three well-known pretrained CNNs, AlexNet, GoogleNet, and ResNet-101, were investigated for accuracy and RFI detection. All networks provided very similar accuracy results for the validation datasets; however, AlexNet provided the best results when used for RFI detection on other test orbits.

The algorithm had high performance for detecting RFI localized in time or frequency and lower performance for broadband RFI. RFI-free data is usually broadband and vary smoothly over long time-scales, while RFI can appear as high-intensity pixels localized in time/frequency data. RFI can also have broadband features and vary over time-scales longer than a footprint. The results show that classification is highly dependent on the type of input data. Training data that used geophysical features such as coastlines produced more missed detections of broadband RFI, while training data without them sometimes mistook coastlines for RFI.

The trained networks were also used to detect DBS signals measured by a K-band system demonstrating that the trained networks can identify RFI in data from other systems. The work in this article presents the initial step to applying deep learning for detection of RFI in radiometer data. To provide better performance for detection of all types of RFI, the training dataset requires more input training data, representative of all types of RFI and geophysical features. To provide better detection especially for RFI with broadband features, the pretrained network can be retrained with a data subset with improved ground truth such as simulated data. Future work includes the development of a comprehensive set of simulated and real-world data of RFI and RFI-free spectrograms with varying RFI resolution and INR to

train a network from scratch. Performance factors to be evaluated include detection capability and energy efficiency. The use of CNNs to detect RFI is an attractive alternative to conventional techniques given the large amount of radiometer data that will exist in the coming decades.

REFERENCES

[1] N. Niamsuwan, J. T. Johnson, and S. W. Ellingson, "Examination of a simple pulse blanking technique for RFI mitigation," *Radio Sci.*, vol. 40, no. 5, pp. RS5S03-1–RS5S03-5, Oct. 2005.

[2] C. S. Ruf, S. M. Gross, and S. Misra, "RFI detection and mitigation for microwave radiometry with an agile digital detector," *IEEE Trans. Geosci. Remote Sens.*, vol. 44, no. 3, pp. 694–706, Mar. 2006.

[3] B. Guner, N. Niamsuwan, and J. Johnson, "Performance study of a cross-frequency detection algorithm for pulsed sinusoidal RFI in microwave radiometry," *IEEE Trans. Geosci. Remote Sens.*, vol. 48, no. 7, pp. 2899–2908, Jul. 2010.

[4] J. E. Balling, S. S. Sobjaerg, S. S. Kristensen, and N. Skou, "RFI detected by kurtosis and polarimetry: Performance comparison based on airborne campaign data," in *Proc. 12th Specialist Meeting Microw. Radiometry Remote Sens. Environ.*, Rome, Italy, Mar. 2012, pp. 1–4.

[5] L. Li, P. W. Gaiser, M. H. Bettenhausen, and W. Johnston, "WindSat radiofrequency interference signature and its identification over land and ocean," *IEEE Trans. Geosci. Remote Sens.*, vol. 44, no. 3, pp. 530–539, Mar. 2006.

[6] L. Li, E. G. Njoku, E. Im, P. S. Chang, and K. S. Germain, "A preliminary survey of radio-frequency interference over the U.S. in aqua AMSR-E data," *IEEE Trans. Geosci. Remote Sens.*, vol. 42, no. 2, pp. 380–390, Feb. 2004.

[7] J. T. Johnson *et al.*, "Airborne radio-frequency interference studies at C-band using a digital receiver," *IEEE Trans. Geosci. Remote Sens.*, vol. 44, no. 7, pp. 1974–1985, Jul. 2006.

[8] D. McKague, J. J. Puckett, and C. Ruf, "Characterization of K-band radio frequency interference from AMSR-E, windsat and SSM/I," in *Proc. IEEE Int. Geosci. Remote Sens. Symp.*, 2010, pp. 2492–2494.

[9] D. Draper and D. Newell, "An assessment of radio frequency interference using the GPM microwave imager," in *Proc. IEEE Int. Geosci. Remote Sens. Symp.*, 2015, pp. 5170–5173.

[10] G. F. Forte, J. Querol, A. Camps, and M. Vall-llossera, "Real-time RFI detection and mitigation system for microwave radiometers," *IEEE Trans. Geosci. Remote Sens.*, vol. 51, no. 10, pp. 4928–4935, Oct. 2013.

[11] D. Entekhabi *et al.*, "The soil moisture active passive (SMAP) mission," *Proc. IEEE*, vol. 98, no. 5, pp. 704–716, May 2010.

[12] J. R. Piepmeier *et al.*, "Radio-frequency interference mitigation for the soil moisture active passive microwave radiometer," *IEEE Trans. Geosci. Remote Sens.*, vol. 42, no. 1, pp. 761–775, Jan. 2014.

[13] P. N. Mohammed, M. Aksoy, J. R. Piepmeier, J. T. Johnson, and A. Bringer, "SMAP L-band microwave radiometer: RFI mitigation prelaunch analysis and first year on-orbit observations," *IEEE Trans. Geosci. Remote Sens.*, vol. 54, no. 10, pp. 6035–6047, Oct. 2016.

[14] M. Ogut *et al.*, "The calibration and stability analysis of the JPL ultra-wide P/L-band radiometer," in *Proc. IEEE Int. Geosci. Remote Sens. Symp.*, Yokohama, Japan, 2019, pp. 8897–8900.

[15] M. Andrews *et al.*, "The ultra-wideband software defined microwave radiometer (UWBRAD) for ice sheet subsurface temperature sensing: Calibration and campaign results," in *Proc. IEEE Int. Geosci. Remote Sens. Symp.*, Fort Worth, TX, USA, 2017, pp. 237–240.

[16] J. Lahtinen *et al.*, "Real-time RFI processor for future spaceborne microwave radiometers," *IEEE J. Sel. Topics Appl. Earth Observ. Remote Sens.*, vol. 12, no. 6, pp. 1658–1669, Jun. 2019.

[17] S. S. Kristensen, N. Skou, S. S. Søbjærg, and J. E. Balling, "Developments of RFI detection algorithms and their application to future European spaceborne systems," in *Proc. IEEE Int. Geosci. Remote Sens. Symp.*, Yokohama, Japan, 2019, pp. 4451–4454.

[18] S. Boukabara and K. Garrett, "Benefits of a hyperspectral microwave sensor," in *Proc. IEEE Sensors*, Limerick, 2011, pp. 1881–1884.

[19] F. Aires *et al.*, "Microwave hyperspectral measurements for temperature and humidity atmospheric profiling from satellite: The clear-sky case," *J. Geophys. Res. Atmos.*, vol. 120, pp. 11334–11351, 2015.

[20] J. Akeret, C. Chang, A. Lucchi, and A. Refregier, "Radio frequency interference mitigation using deep convolutional neural networks," *Astron. Comput.*, vol. 18, pp. 35–39, Jan. 2017.

[21] A. Pérez, J. Querol, H. Park, and A. Camps, "Radio-frequency interference location, detection and classification using deep neural networks," in *Proc. IEEE Int. Geosci. Remote Sens. Symp.*, 2020, pp. 6977–6980.

[22] I. Goodfellow, Y. Bengio, and A. Courville, *Deep Learning*, vol. 1. Cambridge, MA, USA: MIT Press, 2016.

[23] Y.-N. Dong and G.-S. Liang, "Research and discussion on image recognition and classification algorithm based on deep learning," in *Proc. Int. Conf. Mach. Learn. Big Data Bus. Intell.*, Taiyuan, China, 2019, pp. 274–278.

[24] A. Sevik, P. Erdogmus, and E. Yalein, "Font and Turkish letter recognition in images with deep learning," in *Proc. Int. Congr. Big Data, Deep Learn. Fighting Cyber Terrorism*, Ankara, Turkey, 2018, pp. 61–64.

[25] A. Krizhevsky, I. Sutskever, and G. E. Hinton, "ImageNet classification with deep convolutional neural networks," in *Proc. Adv. Neural Inf. Process. Syst.*, 2012, pp. 1097–1105.

[26] Y. Long, Y. Gong, Z. Xiao, and Q. Liu, "Accurate object localization in remote sensing images based on convolutional neural networks," *IEEE Trans. Geosci. Remote Sens.*, vol. 55, no. 5, pp. 2486–2498, May 2017.

[27] L. Shao, F. Zhu, and X. Li, "Transfer learning for visual categorization: A survey," *IEEE Trans. Neural Netw. Learn. Syst.*, vol. 26, no. 5, pp. 1019–1034, May 2015.

[28] C. Szegedy *et al.*, "Going deeper with convolutions," in *Proc. IEEE Conf. Comput. Vis. Pattern Recognit.*, 2015, pp. 1–9.

[29] K. He, X. Zhang, S. Ren, and J. Sun, "Deep residual learning for image recognition," in *Proc. IEEE Conf. Comput. Vis. Pattern Recognit.*, 2016, pp. 770–778.

[30] *ImageNet*. [Online]. Available: http://www.image-net.org.

[31] P. Mohammed-Tano, *Soil Moisture Active Passive (SMAP) Project Level 1A Radiometer Product Specification Document*, JPL-D-92340. Pasadena, CA, USA: Jet Propulsion Lab, 2015. [Online]. Available: https://nsidc.org/sites/nsidc.org/files/technical-references/D-92340-A_SMAP_Radiometer_Level1A_Product_Specification_Document_150720_with%20sigs.pdf

[32] J. R. Piepmeier, *Soil Moisture Active Passive (SMAP) Project Algorithm Theoretical Basis Document*, SMAP L1B Radiometer Data Product: L1B_TB. Pasadena, CA, USA: Jet Propulsion Lab., 2018. [Online]. Available: https://nsidc.org/sites/nsidc.org/files/technical-references/L1BTB_ATBD_RevC_May2018.pdf

[33] S. C. Ho *et al.*, "Wideband ocean altimetry using Ku-band and K-band satellite signals of opportunity: Proof of concept," *IEEE Geosci. Remote Sens. Lett.*, vol. 16, no. 7, pp. 1012–1016, Jul. 2019.

[34] P. N. Mohammed *et al.*, "Detection of radio frequency interference in microwave radiometers operating in shared spectrum," *IEEE Trans. Geosci. Remote Sens.*, vol. 57, no. 9, pp. 7067–7074, Sep. 2019.

[35] D. W. Draper and D. A. Newell, "An assessment of radio frequency interference using the GPM microwave imager," in *Proc. IEEE Geosci. Remote Sens. Symp.*, Milan, Italy, 2015, pp. 5170–5173.

[36] D. W. Draper, D. A. Newell, F. J. Wentz, S. Krimchansky, and G. M. Skofronick-Jackson, "The global precipitation measurement (GPM) microwave imager (GMI): Instrument overview and early on-orbit performance," *IEEE J. Sel. Topics Appl. Earth Observ. Remote Sens.*, vol. 8, no. 7, pp. 3452–3462, Jul. 2015.

Priscilla N. Mohammed (Member, IEEE) received the B.S. degree from Florida Institute of Technology, Melbourne, FL, USA, in 1999, and the M.S. and Ph.D. degrees from Georgia Institute of Technology, Atlanta, GA, USA, in 2001 and 2005, respectively, all in electrical engineering.

She is currently with Goddard Earth Sciences Technology and Research (GESTAR), Universities Space Research Association, Columbia, MD, USA, as a member of the Morgan State University Research Faculty and also with the Microwave Instrument Technology Branch, NASA's Goddard Space Flight Center, Greenbelt, MD, USA. She is currently a member of the Algorithm Development Team for the Soil Moisture Active Passive Radiometer. Her research interests include radio frequency interference mitigation in microwave radiometers.

Dr. Mohammed is also a member of the Technical Committee for Frequency Allocations in Remote Sensing (FARS).

Jeffrey R. Piepmeier (Fellow, IEEE) received the B.S.E. degree in electrical concentration from Le-Tourneau University, Longview, TX, USA, in 1993, and the M.S. and Ph.D. degrees in electrical engineering from Georgia Institute of Technology, Atlanta, GA, USA, in 1994 and 1999, respectively.

He is currently a Chief Engineer for passive microwave instruments with the Instrument Systems and Technology Division, NASA's Goddard Space Flight Center (GSFC), Greenbelt, MD, USA. He is a Deputy Study Coordinator for NASA Aerosols, Clouds, Convection and Precipitation (ACCP) Decadal Survey architecture study, Technology Co-Lead of the NASA Planetary Boundary Layer Decadal Survey Incubation study team, and Instrument Scientist for the SMAP microwave radiometer. He served as an Instrument Subject Matter Expert on the NOAA Satellite Observing System Architecture study. He also contributed to various leadership roles on the cubesat projects IceCube, CubeRRT, and SNOOPI. Previously at GSFC, he was Associate Head, Microwave Instruments and Technology Branch, Instrument Scientist for the GPM Microwave Imager, and Instrument System Engineer for the Aquarius microwave radiometer. Prior to NASA, he worked with Vertex Communications Corp. and was a Shackleford Fellow with the Georgia Tech Research Institute, Atlanta, GA, USA. His research interests include microwave radiometry and technology development to enable the next generation of microwave sensors.

Dr. Piepmeier is a member of URSI (Commission F). He is a past Chairperson of the National Academies' Committee on Radio Frequencies (CORF). He is the recipient of NASA's Exceptional Engineering Achievement Medal, Exceptional Achievement Medal, and Outstanding Leadership Medal; Department of Commerce's NOAA Bronze Medal; and multiple NASA Group Achievement Awards.